Current modulation by voltage control of the quantum phase in crossed graphene nanoribbons

K. M. Masum Habib* and Roger K. Lake†

Department of Electrical Engineering, University of California, Riverside, CA 92521-0204

(Received 3 September 2011; revised manuscript received 24 May 2012; published 11 July 2012)

A relative rotation of 90° between two graphene nanoribbons (GNRs) creates a crossbar with a nanoscale overlap region. Calculations, based on the first principles density functional theory (DFT) and the nonequilibrium Green's function (NEGF) formalism, show that the electronic states of the individual GNRs of an unbiased crossbar are decoupled from each other similar to the decoupling that occurs in twisted bilayer graphene. Analytical calculations, based on Fermi's golden rule, reveal that the decoupling is a consequence of the cancellation of quantum phases of the electronic wave functions of the individual GNRs. As a result, the inter-GNR transmission is strongly suppressed over a large energy window. An external bias applied between the GNRs changes the relative phases of the wave functions resulting in modulation of the transmission and current by several orders of magnitude. A built-in potential between the two GNRs can lead to a large peak-to-valley current ratio (>1000) resulting from the strong electronic decoupling of the two GNRs that occurs when they are driven to the same potential. Current switching by voltage control of the quantum phase in a graphene crossbar structure is a novel switching mechanism. It is robust even with an overlap of ∼1.8 nm × 1.8 nm that is well below the smallest horizontal length scale envisioned in the international technology roadmap for semiconductors (ITRS).

DOI: 10.1103/PhysRevB.86.045418 PACS number(s): 72.80.Vp

I. INTRODUCTION

Lack of a band gap in graphene[1,2] is one of the challenges for achieving high ON/OFF current ratios in graphene field effect transistors (FETs). The most obvious way to circumvent this problem is to open a band gap, e.g., by using chemical doping,[3] creating nanoribbons,[4–6] or by applying a vertical electric field in bilayer graphene.[7–9] However, it is difficult to create a sufficiently large band gap without degrading the electronic properties of graphene. Another way is to utilize the unique properties of graphene in alternative FET architectures.[10–13] A highly nonlinear current-voltage relationship can be obtained in a graphene-insulator-graphene *p-n* junction.[14] Some devices exhibiting negative differential resistance (NDR) have been proposed.[15–19] However, most of these devices have relatively complex architectures,[12,13,15–17] limited scalability,[10] or low on-off or peak-to-valley current ratios.[17–19] In this work, we unveil a current switching mechanism in graphene crossbars in which the current can be modulated by several orders of magnitude. This switching mechanism is based on voltage control of the relative phases of the electronic wave functions of two crossed graphene nanoribbons. It does not rely on a band gap, and it is not based on tunneling through or over a potential barrier. It is relatively independent of temperature. It is robust even when the overlap of the active region is scaled down to ∼1.8 nm × 1.8 nm. This length scale is well below any horizontal scale envisioned in the ITRS.[20]

Interest in twisted, or misoriented, layers of graphene was recently motivated by the need to understand the electronic properties of multilayer graphene furnace grown on the C face of SiC.[21] Experimental analysis showed that the layers tended to be rotated with respect to each other at certain angles corresponding to allowed growth orientations with respect to the SiC substrate.[22] Calculations, based on density functional theory,[21–24] empirical tight-binding,[25] and continuum[26] models for such rotated bilayers found linear dispersion near the K points. A recent experiment showed that in twisted bilayer graphene for twist angles greater than ∼3°, the low-energy carriers behave as massless Dirac fermions with a reduced Fermi velocity compared to that of single-layer graphene, and that for twist angles greater than 20°, the layers are effectively decoupled and act as independent layers.[27] A vertical electric field in a twisted bilayer graphene can couple the layers[28] and reduce the Fermi velocity.[29] A recent study of the conductivity between two infinite rotated sheets of graphene found enhanced conductance at commensurate angles with relatively small unit cells and negative differential resistance at small biases.[30]

Although the physics of the decoupled layers in twisted bilayer graphene has been studied extensively, it is not clear if these properties still hold in the limit of nanoscaled device dimensions, for example, in the twisted bilayer that occurs in the overlap region of two crossed GNRs fabricated by unzipping two carbon nanotubes.[31] Botello-Méndez *et al.* very recently addressed this issue performing both DFT and empirical tight-binding calculations of the transmission across and through crossed graphene nanoribbons.[32] Crossed armchair-zigzag (AZ) GNRs and crossed zigzag-zigzag GNRs were considered. Most relevant to our work, was their study of crossed AZ GNRs, approximately 5-nm wide, aligned in AB stacking at right angles and then rotated. The minimum in the interlayer transmission between the armchair GNR (aGNR) and the zigzag GNR occurred when the angle of intersection was 60°. This is equivalent to the 90° angle of intersection between two aGNRs, which is the system that we consider.

In this work, we analyze the physical mechanism of the interlayer coupling at the nanoscale and its dependence on the potential difference between the two layers, and we show that it can be exploited for current switching by voltage control of the wave function phase. The model structure shown in Fig. 1 consists of two armchair GNRs with one placed on top of the other at right angles forming a GNR crossbar (xGNR). In this case, the overlap region of the xGNR, which is neither AA nor AB stacking, is a twisted bilayer with an area of

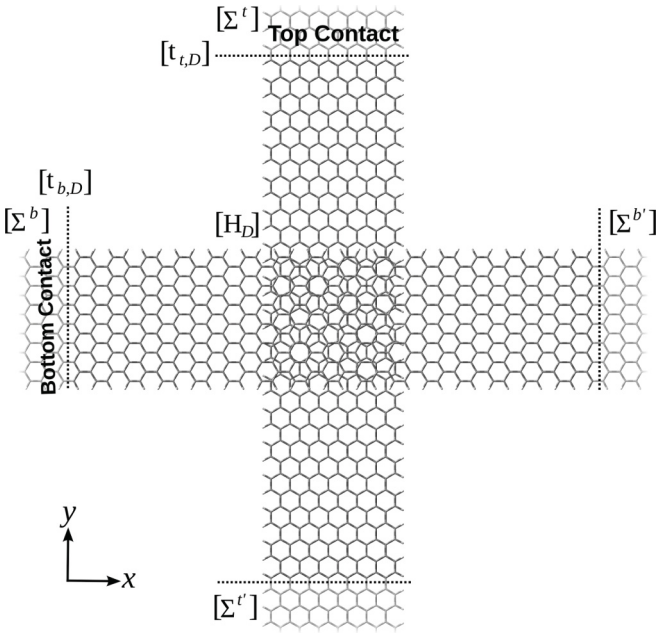

FIG. 1. Atomistic geometry of the crossbar GNR (xGNR) consisting of two H-passivated armchair GNRs with one placed on top of the other rotated by 90°. Each GNR is 14-C atomic layers wide (∼1.8 nm) with a band gap of 130 meV. The contacts are modeled by the self-energies of semi-infinite leads. The region bounded by the broken lines is used as a supercell for the band structure calculations.

∼1.8 nm × 1.8 nm and a twist angle of 90°. For two infinite sheets, a 90° rotation is the same as a 30° rotation which is not a commensurate rotation angle. A Moiré pattern can be observed at the intersection of the two nanoribbons in Fig. 1.

Calculations, based on *ab initio* density functional theory (DFT) coupled with the nonequilibrium Green's function formalism (NEGF), show that the interlayer decoupling still exists in such a small geometry containing approximately 220 C atoms leading to strong suppression of inter-GNR transmission when the two layers are at the same potential. An analytical model using Fermi's golden rule reveals that the suppression of the interlayer transmission results from the cancellation of the quantum phases of the electronic wave functions of the individual GNRs. An external bias applied between the GNRs changes the relative phases of the wave functions resulting in modulation of the transmission and current by several orders of magnitude. The decoupling that occurs when the GNRs are at equal potentials can be exploited using a built-in potential similar to the one that occurs in a *p-n* junction to produce negative differential resistance with a large (>1000) peak-to-valley current ratio. A large, dense array of crossed graphene nanoribbons, with each cross point providing a nonlinear current-voltage response, could serve in, for example, a cellular neural network,[33] a memory array,[34] or provide added functionality to standard transistor circuits.[35] While in this paper, we consider a two-terminal configuration, one could also control the interlayer potential with gates, in which case the physics described here could be exploited to implement ultrascaled transistors.

II. METHOD

In this study, four different types of calculations are performed. (i) Geometry optimization and (ii) band structure calculations are performed using DFT. (iii) The electronic transport of the xGNR is calculated using the NEGF formalism coupled with DFT. (iv) The numerical results are explained using analytical expressions for the wave functions in a π-orbital basis. The calculation methods and the device structure are discussed below.

A. Device structure

The crossbar structure consists of two H-passivated, armchair GNRs shown in Fig. 1. In this arrangement, the GNR along the y axis is placed on top of the GNR along the x axis with a vertical separation of 3.35 Å in between. Throughout the rest of the paper, the GNRs placed along x and y axes will be referred to as the "bottom" and "top" GNRs, respectively. Since we are interested in current modulation in the absence of a band gap, the widths of the GNRs are chosen to be 14-C atomic layers $(3n+2) \sim 1.8$ nm to minimize the band gap resulting from the finite width. The band gap of the 14-aGNR, calculated from DFT code FIREBALL[36,37] is 130 meV, which is in good agreement with Son *et al.*[38] The area of the overlap region of the xGNR is ∼1.8 nm × 1.8 nm. The total simulated area between the four ideal leads indicated by the self-energies in Fig. 1 is ∼7 nm × 7 nm.

The infinite xGNR, shown in Fig. 1, is constructed by attaching the self-energies $\mathbf{\Sigma}^t$ and $\mathbf{\Sigma}^{t'}$ to the top GNR and the self-energies $\mathbf{\Sigma}^b$ and $\mathbf{\Sigma}^{b'}$ to the bottom GNR. Throughout this article, the semi-infinite leads indicated by the self-energies $\mathbf{\Sigma}^t$ and $\mathbf{\Sigma}^b$ are termed as top and bottom contacts respectively.

B. FIREBALL

The geometry optimization and the calculation of electronic structures are performed with the *ab initio* quantum mechanical molecular dynamics, DFT code FIREBALL[36,39] using separable, nonlocal Troullier-Martins pseudopotentials,[40] the BLYP exchange correlation functional[41,42] and a self-consistent generalization of the Harris-Foulkes energy functional.[43–47] A single zeta (single numeric) sp^3 FIREBALL basis set is used. These localized pseudoatomic orbitals are slightly excited due to hard wall boundary conditions imposed at radial cutoffs, r_c, for each atomic species. The cutoffs are $r^{1s} = 4.10$ Å for hydrogen and $r^{2s} = 4.4$ Å, and $r^{2p} = 4.8$ Å for carbon.[48]

C. Structure relaxation

In order to construct the crossbar, the geometry of a supercell of H-passivated single layer aGNR with periodic boundary conditions is optimized using FIREBALL. The supercell, which has a length of eight atomic layers, is repeated using the lattice vector $\vec{a} = 8.77\hat{x}$ (Å). The relaxation is performed until all the Cartesian forces on the atoms are <0.05 eVÅ^{-1}. In the self-consistent field calculation, a Fermi smearing temperature of 50 K and self-consistent convergence factor of 10^{-7} are used. The one-dimensional Brillouin zone is sampled using $8k$ points during optimization. This relaxed single-layer supercell is then repeated to construct longer GNR

which, in turn, is used to construct the crossbar. No further relaxation is performed for crossbar.

D. Band structure

The region indicated by the broken lines in Fig. 1 forms the crossbar supercell for electronic band structure calculations. The supercell is repeated with lattice vectors $\vec{a}_1 = 7.016\hat{x}$ and $\vec{a}_2 = 7.016\hat{y}$ (nm). For the self-consistent field calculation, the first Brillouin zone is sampled using a Monkhorst-Pack scheme with a k mesh of 7×7. The electronic structure of the supercell is calculated with FIREBALL using the basis, pseudopotentials, functional, Fermi smearing temperature, and convergence factor as described above.

E. Transport

The Hamiltonian matrix elements used in the NEGF calculation are generated from the FIREBALL super-cell calculation. The matrix elements include the electron-electron interaction at the DFT/BLYP level of theory in equilibrium. The matrix elements of the external applied potential U are calculated as $\langle i,\alpha|U|j,\beta\rangle = S_{\alpha_i,\beta_j}[U(\mathbf{r}_i) + U(\mathbf{r}_j)]/2$ where the indices i and j label the atoms, the indices α and β label the basis orbitals, and S_{α_i,β_j} is the overlap matrix $\langle i,\alpha|j,\beta\rangle$. This approach in which the matrix elements of the external potential have the same form as in an extended Hückel model has been used by others.[49] The approach captures the Stark effect, but not *nonequilibrium* charge self-consistency. The applied bias V is distributed symmetrically between the top and the bottom GNRs such that the electrostatic potential energies are $U(\mathbf{r}_i) = -eV/2$ for atoms on the top GNR and, $U(\mathbf{r}_i) = eV/2$ for atoms on the bottom GNR.

The matrix elements are used in a recursive Green's function (RGF) algorithm that utilizes nonuniform block layers to calculate the Green's function of the device, $\mathbf{G}^R$, as described in Ref. 48. The self-energies $\mathbf{\Sigma}^t$ and $\mathbf{\Sigma}^b$ are calculated with the decimation method[50] using a 10 meV broadening factor. The transmission spectrum $T(E)$ is then calculated from the standard Green's function expression, $T(E) = \mathrm{tr}\{\mathbf{\Gamma}^b_{1,1}\mathbf{G}^R_{1,N}\mathbf{\Gamma}^t_{N,N}(\mathbf{G}^R_{1,N})^\dagger\}$, where the indices 1 and N indicate the first and last block-layers of the xGNR, respectively, $\mathbf{\Gamma}^b_{1,1} = i(\mathbf{\Sigma}^b - \mathbf{\Sigma}^{b\dagger})$, and $\mathbf{\Gamma}^t_{N,N} = i(\mathbf{\Sigma}^t - \mathbf{\Sigma}^{t\dagger})$. The coherent current is calculated from

$$I = \frac{2e}{\hbar}\int \frac{dE}{2\pi} T(E)[f(E-(\mu+eV/2)) - f(E-(\mu-eV/2))], \quad (1)$$

where $f(E)$ is the Fermi function and μ is the equilibrium Fermi level. The temperature is 300 K for all current calculations.

F. Analytical model

An expression for the current flow between the two GNRs can also be obtained from Fermi's golden rule using analytical expressions for the wave functions and empirical tight-binding parameters for the matrix elements. The transition rate from a k_x state of mode n in the bottom GNR to a k_y state of mode m in the top GNR is

$$\frac{1}{\tau} = \frac{2\pi}{\hbar}|M_{mn}(k_x,k_y)|^2\delta(E_m(k_y) - 2U - E_n(k_x)), \quad (2)$$

where $E_i(k)$ is the energy-wave-vector relation of an individual GNR for mode i. $U = eV/2$ is the magnitude of the electrostatic potential energies of the individual GNRs. The matrix element M_{mn} is calculated between the k_x state on the bottom GNR and the k_y state on the top GNR, and the detailed expression is given below in Eq. (13). The current is obtained by multiplying Eq. (2) with the Fermi factors of the top and bottom contacts $[f(E_n - (\mu + U)) - f(E_m - (\mu - U))]$ and summing over all initial and final states. The sum over k_x and k_y gives the joint density of states of the top and bottom GNR,

$$\sum_{k_x,k_y}\delta(E_m(k_y) - 2U - E_n(k_x)) = \int dE N^n_{1D}(E-U)N^m_{1D}(E+U), \quad (3)$$

where N^i_{1D} is the single-spin, 1D density of states for mode i that has the units of (energy^{-1}). The final expression for the current is

$$I = \frac{4\pi e}{\hbar}\sum_{m,n}\int dE|M_{mn}|^2 N^n_{1D}(E-U)N^m_{1D}(E+U) \times [f(E-(\mu+U)) - f(E-(\mu-U))], \quad (4)$$

which has the same form as the equation for current obtained for 2D twisted bilayer graphene.[30] Comparing Eq. (1) with Eq. (4) gives the analytical expression for the transmission,

$$T(E) = 4\pi^2\sum_{m,n}|M_{mn}|^2 N^n_{1D}(E-U)N^m_{1D}(E+U). \quad (5)$$

The expression for the matrix element M_{mn} can be obtained from the expression for the electronic wave function of a single-layer aGNR as follows. The energy-wave-vector dispersion relationship of band n of an N-atomic layers wide aGNR can be written as[51]

$$E_n(k) = \epsilon + \mathrm{sgn}(n)|\tilde{t}_n(k)| \quad (6)$$

with

$$\tilde{t}_n(k) \equiv \langle\psi_{nkA}|H|\psi_{nkB}\rangle = -t_0[2e^{ika_{cc}/2}\cos(\theta_n) + e^{-ika_{cc}}], \quad (7)$$

where ϵ is the site energy of the carbon atoms, k is the wave vector, sgn is the signum function, t_0 is the in-plane nearest-neighbor hopping parameter, a_{cc} is the C-C bond length, and $\theta_n = \frac{|n|\pi}{N+1}$. The corresponding electronic wave function is given by[51]

$$|\psi_{nk}\rangle = \frac{1}{\sqrt{2}}(|\psi_{nkA}\rangle + \mathrm{sgn}(n)e^{-i\Theta_{nk}}|\psi_{nkB}\rangle) \quad (8)$$

with

$$\Theta_{nk} = \angle\tilde{t}_n(k) \quad (9)$$

and

$$|\psi_{nk\alpha}\rangle = \sqrt{\frac{2}{N_x(N+1)}}\sum_{p=1}^{N}\sum_{q=1}^{N_x}e^{ikx_q}\sin(\theta_n p)|\alpha_{pq}\rangle, \quad (10)$$

where $\alpha \in \{A,B\}$ represents the A or B atomic sites, p and q count the atomic layers and the unit cells, respectively, and N_x is the total number of unit cells considered. $|\alpha_{pq}\rangle$ is the p_z orbital of the atomic site α in the unit cell q and atomic layer p of the GNR. The matrix element M_{mn} can be resolved into four components,

$$M_{mn} \equiv \langle \psi_{mk_y} | H_{\rm int} | \psi_{nk_x} \rangle \tag{11}$$

$$= M_{mn}^{AA} + M_{mn}^{AB} + M_{mn}^{BA} + M_{mn}^{BB} \tag{12}$$

$$= \frac{1}{2} \sum_{\alpha=A,B} \sum_{\beta=A,B} C_{mn}^{\alpha\beta} H_{mn}^{\alpha\beta}, \tag{13}$$

where

$$C_{mn}^{AA} = 1, \tag{14}$$

$$C_{mn}^{AB} = \mathrm{sgn}(n) e^{-i\Theta_{nk_x}}, \tag{15}$$

$$C_{mn}^{BA} = \mathrm{sgn}(m) e^{i\Theta_{mk_y}}, \tag{16}$$

$$C_{mn}^{BB} = C_{mn}^{AB} C_{mn}^{BA} = \mathrm{sgn}(nm) e^{i(\Theta_{mk_y} - \Theta_{nk_x})}, \tag{17}$$

and

$$H_{mn}^{\alpha\beta} \equiv \langle \psi_{mk_y\alpha} | H_{\rm int} | \psi_{nk_x\beta} \rangle \tag{18}$$

$$= \frac{2}{\sqrt{N_x N_y}(N+1)} \sum_{p=1}^{N} \sum_{q=1}^{N_y} \sum_{p'=1}^{N} \sum_{q'=1}^{N_x} e^{i(k_x x_{q'} - k_y y_q)} \times \sin(\theta_m p) \sin(\theta_n p') \langle \alpha_{pq} | H_{\rm int} | \beta_{p'q'} \rangle, \tag{19}$$

where $H_{\rm int}$ is the inter-GNR interaction, p and q are the indices of the atoms of the top GNR, and p' and q' are the indices of the the atoms of the bottom GNR. The quantity $\langle \alpha_{pq} | H_{\rm int} | \beta_{p'q'} \rangle$ is calculated using the empirical formula[28]

$$\langle \alpha_{pq} | H_{\rm int} | \beta_{p'q'} \rangle = -t_1 e^{-3(d_{pqp'q'} - d_o)}, \tag{20}$$

where t_1 is the nearest-neighbor interlayer hopping parameter, $d_{pqp'q'}$ is the distance between the atoms on the top and the bottom GNRs, and d_o is the inter-GNR distance. The edge effects were taken into account by replacing $\tilde{t}_n(k)$ in Eq. (9) by $\tilde{t}_n(k) + \delta\tilde{t}_n(k)$ where $\delta\tilde{t}_n(k)$ is the correction for the edge bonds following Ref. 51. While calculating M_{mn}, the site energies of the C atoms of the top and the bottom GNRs are rigidly shifted by $-eV/2$ and $eV/2$, respectively, to include the effects of the external bias voltage V.

For all the calculations presented below, the hopping parameters are $t_0 = 3.16$ eV and $t_1 = 0.39$ eV.[28] For the 14 atomic layer aGNR ($N = 14$), the conduction-band subband index is $n = 10$, and the valance-band subband index is $n = -10$.

III. NUMERICAL RESULTS

A. Band structure

The band structure of the crossbar supercell, calculated as described in Sec. II D using the DFT code FIREBALL, reveals that the low-energy states of the top and the bottom GNRs are electronically decoupled. The calculated band gap of the xGNR is found to be ~130 meV, which is equal to the band gap of a single aGNR. The low-energy electronic dispersion

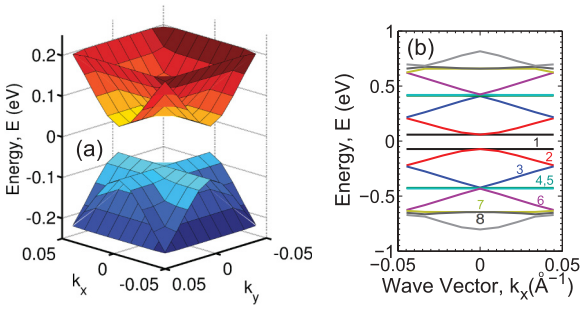

FIG. 2. (Color online) Band structure of the xGNR supercell calculated using FIREBALL (a) as a function of k_x and k_y and (b) as a function of k_x only, at $k_y = 0$. The energy $E = 0$ eV is set at the Fermi level. The bands shown in (a) appear as a superposition of bands of two isolated GNRs with one aligned in the x and the other in y direction. The bands indicated by 1 and 2 in (b) are degenerate at Γ indicating that they are decoupled.

of the xGNR as a function of wave vectors k_x and k_y shown in Fig. 2(a) appears as a superposition of the band structures of two infinite single aGNRs with one placed along the x axis and the other along the y axis. To see this in more detail, the electronic dispersion is plotted as a function of k_x (at $k_y = 0$) in Fig. 2(b). The band indicated by 1 in Fig. 2(b) does not have any dependence on k_x, while band 2 is exactly the same as the valence band of an isolated GNR along the x axis. These two bands are degenerate at Γ that indicates that they are decoupled from each other. This is confirmed by the 3D contour plots of the population at Γ for bands 1 and 2 shown in Figs. 3(a) and 3(b), respectively. Bands 1 and 2 are entirely localized on the top and bottom GNRs, respectively. Therefore bands 1 and 2 correspond to the valance bands of the top and bottom GNRs, respectively. The decoupling is also consistent with recent experimental[27] and theoretical[24] studies of twisted bilayer graphene.

Coupling is observed between the fundamental modes and the first excited modes. Bands 3 and 6 in Fig. 2(b) are the folded valance bands of the the bottom GNR. Similarly, the bands 4 and 5 are the folded valance bands of the top GNR. Bands 7 and 8 are the first excited bands of the top and bottom GNRs. At these energies, splitting is seen at the supercell Brillouin zone edge. These are the energies where the transmission becomes non-negligible. Similar analysis applies for the first excited conduction bands.

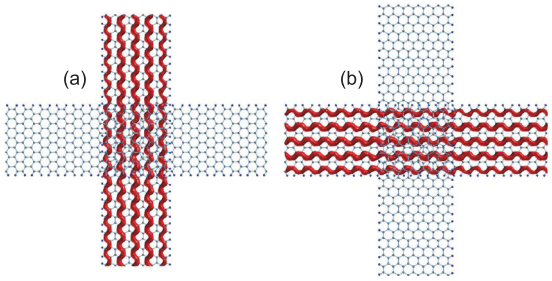

FIG. 3. (Color online) Three-dimensional isosurface of the eigenstate corresponding to (a) band 1 and (b) band 2 in Fig. 2(b) at Γ. The eigenstate of band 1 is localized on the top GNR, and the eigenstate of band 2 is localized on the bottom GNR.

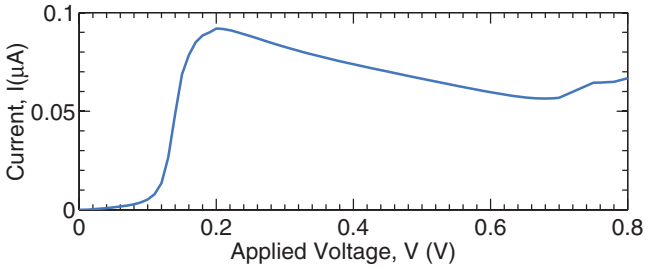

FIG. 4. (Color online) Current voltage (I-V) characteristic of the intrinsic xGNR.

B. Transport

1. Intrinsic xGNR

The simulated current voltage (I-V) characteristic of the xGNR corresponding to Fig. 1 is shown in Fig. 4. Initially, the current increases sharply with the bias, reaches a peak at ∼0.2 V and then decreases exhibiting NDR. The origin of this nonlinear behavior can be understood in terms of the inter-GNR transmission plotted in Fig. 5. The transmission in the unbiased xGNR shown in Fig. 5(a) is strongly suppressed in a large energy window due to the decoupling of the fundamental modes. The asymmetry in the transmission is consistent with the fact that the electron-hole symmetry is broken in bilayer graphene. The peaks near ±0.65 and ±0.9 eV are due to the excited subbands. When the bias voltage is increased beyond the band gap, e.g., at $V = 0.15$ V, the transmission within the energy window defined by the chemical potentials of the top and the bottom contacts increases several orders of magnitude as shown in Fig. 5(b). The transmission between the chemical potentials remains high until $V \sim 0.2$ V, and then it decreases resulting in NDR. The analysis in Sec. IV will show that

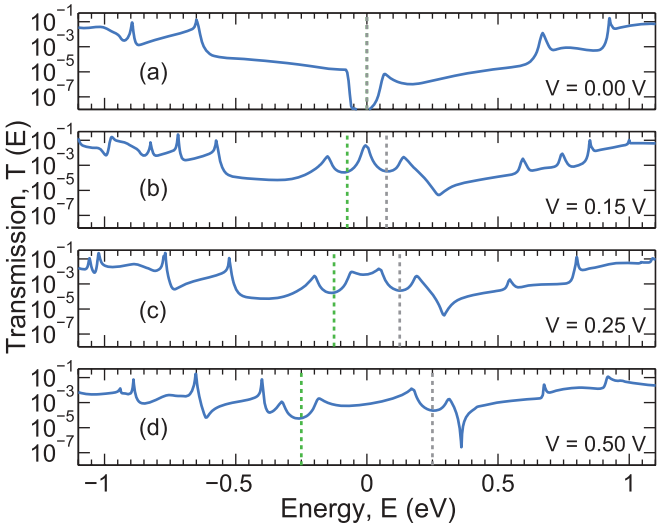

FIG. 5. (Color online) Transmission as a function of energy for different bias voltages. The energy $E = 0$ eV is set at the equilibrium Fermi level. The vertical lines represent the chemical potentials of the top and the bottom contacts. The dips in the transmission near the vertical lines correspond to energies lying inside the band gap of either the top or the bottom GNR. The transmission does not go to zero at these energies as a result of the finite energy broadening used to calculate the surface self-energies of the contacts.

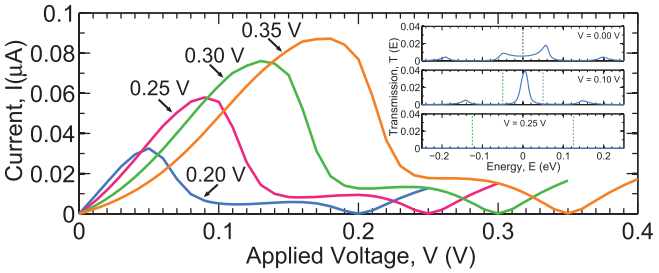

FIG. 6. (Color online) Simulated I-V characteristics of xGNR p-n junctions with different built-in potentials. Inset: Transmission of the xGNR p-n junction for $\phi_{bi} = 0.25$ V as a function of energy for different bias voltages. The energy $E = 0$ eV is set at the equilibrium Fermi level. The vertical lines represent the chemical potentials of the top and bottom contacts.

the dependence of the transmission on the voltage difference between the two GNRs results from voltage control of the relative phases of the top and bottom GNR wave functions. The most important point to take away from the transmission plots in Fig. 5 is that the transmission is suppressed by several orders of magnitude when the potential difference between the GNRs at the cross point is zero.

2. xGNR p-n junction

The strong decoupling of the top and bottom GNR at zero bias can be exploited by creating a built-in potential using either field effect[52,53] or chemical[54,55] doping. For simplicity, we assume that the built-in potentials of the p-doped top GNR and n-doped bottom GNR are $-\phi_{bi}/2$ and $+\phi_{bi}/2$, respectively, where ϕ_{bi} is the total built in potential. The bias V is symmetrically distributed between the GNRs such that the electrostatic potential energies of the top and the bottom GNR are $U = -e(V - \phi_{bi})/2$ and $U = e(V - \phi_{bi})/2$, respectively, and the potential difference between the GNRs is $\Delta U = e(V - \phi_{bi})$.

In Fig. 6, the calculated I-V's through the xGNR are shown for different built in potentials. All of the I-V's show large peak-to-valley current ratios summarized in Table I. The origin of such large peak-to-valley current ratios can be understood by looking at the transmission plots when $\phi_{bi} = 0.25$ V as shown in the inset of Fig. 6. The built-in potential of 0.25 eV between the two GNRs results in a large transmission coefficient at zero bias. Increasing the bias to $V = 0.10$ V decreases the potential energy difference ΔU between the GNRs to 0.15 eV and increases the difference of the chemical potentials of the leads to 0.10 V. The current is proportional to the area under the transmission curve between the two chemical

TABLE I. Calculated peak and valley currents for different built-in potentials for xGNR p-n junction.

ϕ_{bi} (V)	V_{peak} (V)	V_{valley} (V)	I_{peak} (nA)	I_{valley} (pA)	I_{peak}/I_{valley}
0.20	0.05	0.20	32.5	34.4	945
0.25	0.09	0.25	57.9	54.8	1057
0.30	0.13	0.30	76.1	82.2	926
0.35	0.18	0.35	87.2	118.4	737

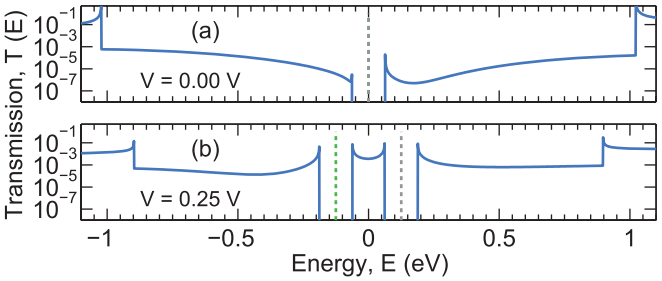

FIG. 7. (Color online) Transmission as a function of energy for different bias voltages calculated using Eq. (5). The energy $E = 0$ eV is set at the equilibrium Fermi level. The dashed vertical lines represent the chemical potentials of the top and the bottom contacts. The gaps in the transmission near the chemical potentials correspond to energies lying inside the band gap of either the top or the bottom GNR. Since the analytical calculations include no energy broadening, the transmission is zero at those energies.

potentials. Increasing the bias drives the potential difference ΔU between the two GNRs to zero. At $V = 0.25$ V, the potential difference between the GNRs becomes zero resulting in strong suppression of the transmission over a large energy window and strong suppression of current. Thus the large peak-to-valley current ratios result from the strong modulation of the transmission with voltage. The physical mechanism governing the voltage dependence of the transmission is analyzed in the next section.

IV. ANALYSIS

The inter-GNR transmission calculated from the analytical expression given by Eq. (5) captures the essential physics of the transmission and its dependence on the potential difference of the two GNRs. The transmission calculated from Eq. (5) is plotted in Fig. 7 for two different biases with $\phi_{\rm bi} = 0$ corresponding to Figs. 4 and 5. At $V = 0$ V, the transmission is strongly suppressed in the energy range between the edges of the first excited subbands, which is in agreement with the numerical calculations. The analytical calculations also capture the asymmetry in the transmission and the voltage modulation of the transmission. For example, at 0.25 V, the transmission inside the energy window bounded by the chemical potentials in Fig. 7(b) increases several orders of magnitude. The gaps in the transmission correspond to energies lying inside the band gap of either the top or the bottom GNR. Since the analytical calculations include no energy broadening, the transmission is zero at those energies.

Although Eq. (5) clearly shows that the transmission is proportional to both the magnitude of the matrix element squared and the joint density of states of the two GNRs, the physics governing the transmission at low energies between the fundamental modes is primarily determined by the matrix element. For example, at $V = 0$ V, the matrix element squared closely resembles the trend in the transmission at low energies as shown by the black curve in Fig. 8(a). The joint 1D density of states peaks at the band edges and, therefore, enhances the transmission at the band edges. Similarly, the matrix element squared at $V = 0.25$ V shown by the black curve in Fig. 8(b) captures the main features of the transmission at low energies

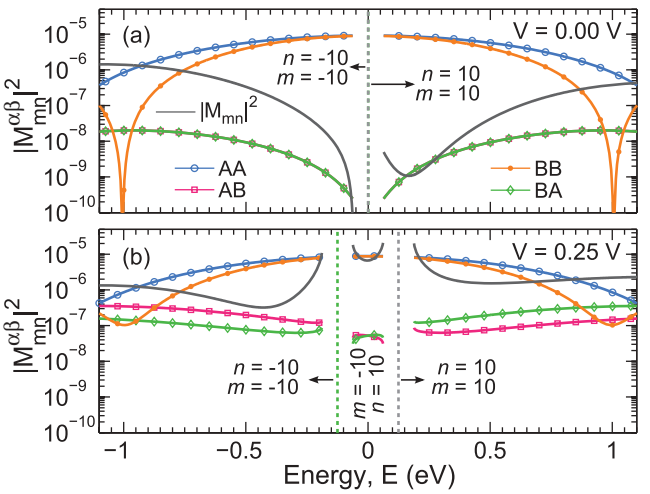

FIG. 8. (Color online) Magnitude squared of the matrix element and its four components considering only the fundamental modes. The total matrix element squared and its components are indicated according to the legend in (a). (a) $V = 0$ V. For $E \gtrsim 0$ eV, $m = 10$ and $n = 10$ and for $E \lesssim 0$ eV, $m = -10$ and $n = -10$. (b) $V = 0.25$ V. For $-0.06 < E < 0.06$ eV, $m = -10$ and $n = 10$; for $E < -0.19$ eV, $m = -10$ and $n = -10$; and for $E > 0.19$ eV, $m = 10$ and $n = 10$. The AB and BA components are very small at low energies near $E = 0$ compared to the AA and BB components in both cases. The vertical lines represent the chemical potentials of the contacts.

and its enhancement by the applied bias. Hence the matrix element governs the voltage dependence of the transmission, and we shall concentrate only on M_{mn} below. In the discussion below, we shall only consider the fundamental modes and hence drop the subscript of M.

The matrix element consists of four components, $M = M^{AA} + M^{BB} + M^{AB} + M^{BA}$ as given by Eq. (12). These four components plotted in Fig. 8 are labeled as "AA," "BB," "AB," and "BA." At low energies, $M \approx M^{AA} + M^{BB}$, since M^{AA} and M^{BB} are orders of magnitude larger than M^{AB} and M^{BA} for all bias voltages.

The cancellation of the phases of M^{AA} and M^{BB} suppresses the matrix element and hence the transmission at $V = 0$ V. This can be understood by looking at the phasor diagram, Fig. 9(a), where the matrix element and its four components are shown in polar coordinates at the conduction band edge. The magnitude of M is very small since $|M^{AA}| \approx |M^{BB}|$ and $\angle M^{AA} - \angle M^{BB} \approx 180^\circ$.

The applied bias does not change $|M^{AA}|$ and $|M^{BB}|$, but it modulates the phase difference between these components which, in turn, results in a significant change in the magnitude of the total matrix element, M. For example, at $V = 0.25$ V, the magnitudes of M^{AA} and M^{BB} shown in Fig. 8(b) remain unchanged. Although $|M^{AB}|$ and $|M^{BA}|$ increase by an order of magnitude, they are still several orders of magnitude smaller compared to $|M^{AA}|$ and $|M^{BB}|$ and hence insignificant. The applied bias changes $\angle M^{BB}$ by $\sim 60^\circ$, while leaving $\angle M^{AA}$ almost unchanged as shown in Fig. 9(b). Thus a bias voltage of 0.25 V changes the phase difference, $\angle M^{AA} - \angle M^{BB}$ from 180° to $\sim 120^\circ$. As a consequence, the total matrix element $M \approx M^{AA} + M^{BB}$ and the resulting transmission increase by several orders of magnitude.

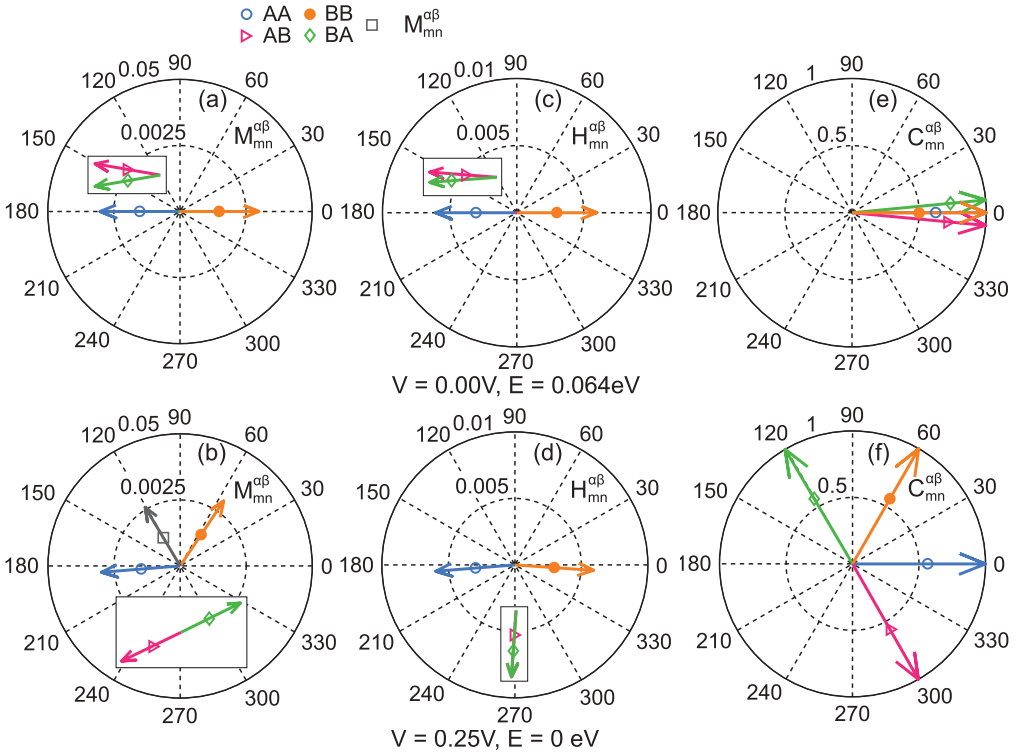

FIG. 9. (Color online) Phasor plots of $M^{\alpha\beta}_{mn}$ (a,b), $H^{\alpha\beta}_{mn}$ (c,d), and $C^{\alpha\beta}_{mn}$ (e,f). The AA, BB, AB, and BA components are indicated according to the legend at the top of the figure. (a), (c), and (e) $V = 0$ V and $E = 0.064$ eV (the conduction band edge). (b), (d), and (f) $V = 0.25$ V and $E = 0$ eV. The lengths and the directions of the arrows represent the magnitude and the angle of the corresponding complex quantities, respectively. Since the AB and BA components of H and M are very small, they are magnified several orders of magnitude and shown in the insets.

The voltage modulation of the phases of the major components $M^{\alpha\alpha} = \frac{1}{2} C^{\alpha\alpha} H^{\alpha\alpha}$ is controlled by the voltage dependent quantum phase factors $C^{\alpha\alpha}$ defined by Eqs. (14) and (17). Figures 9(c) and 9(d) clearly show that the phases of H^{BB} and H^{AA} are only slightly modified by the bias. On the other hand, it is clear from Figs. 9(e) and 9(f) that the bias changes the phase of C^{BB} by $\sim 60^\circ$. The phase of C^{AA} remains unchanged for all energies and for all biases due to the particular construction of the wave function given by Eq. (8). Thus the voltage dependency of the quantum phases are lumped into the quantity C^{BB}.

The asymmetry in transmission at zero bias results from the phase factors C^{AB} and C^{BA} and the small difference between $|M^{AA}|$ and $|M^{BB}|$. At the conduction band edge, $n = 10$ and hence $\angle C^{AB} = \angle\, \mathrm{sgn}(n) e^{-i\Theta_{nk_x}} = -\Theta_{nk_x}$, where Θ_{nk_x} is a small angle. At the valance band edge, $n = -10$ and hence $\angle C^{AB} = \angle\, \mathrm{sgn}(n) e^{-i\Theta_{nk_x}} = 180^\circ - \Theta_{nk_x}$. Thus $\angle C^{AB}$ and hence $\angle M^{AB}$ at the conduction and valence band edges differ by 180°. The same is true for the phase of C^{BA} and M^{BA}. The sum of M^{AB} and M^{BA} adds to M^{AA} at the conduction band edge as shown in Fig. 9(a), and the sum adds to M^{BB} at the valence band edge. $|M^{AA}|$ is slightly larger than $|M^{BB}|$. At the valence band edge, the addition of $(M^{AB} + M^{BA})$ to M^{BB} gives a better cancellation with M^{AA} resulting in the matrix element minimum shown in Fig. 8(a). At the conduction band edge, the addition of $(M^{AB} + M^{BA})$ to M^{AA} reduces the cancellation with M^{BB} resulting in a larger total matrix element and increased transmission.

In a preliminary study of the sensitivity of the transport properties to the detailed geometry of the overlap region, we have considered four variations of the xGNR shown in Fig. 1: the x and the y coordinates of the top GNR are shifted by (a) $a_{cc}/2$ and (b) $3a_{cc}/2$, (c) the width of both arms are increased to 4.5 nm (38 atomic C layers), and (d) the width of the top GNR is increased to 20 C atoms so that the xGNR consists of a 14-aGNR and a 20-aGNR. Calculations, based on the model presented in Sec. II F, show that the transport properties of all of these xGNRs are similar to that of the crossbar shown in Fig. 1. The I-V characteristics of these xGNRs with the biasing scheme described in Sec. III B2 are all similar to the I-V's shown in Fig. 6. The peak-to-valley current ratios for the (a), (b), (c), and (d) configurations at $\phi_{\mathrm{bi}} = 0.25$ V are 100, 1000, 150, and 120, respectively.

V. CONCLUSIONS

We have performed *ab initio* DFT and NEGF based calculations to study the inter-layer coupling and transport properties of nanometer scale twisted bilayer graphene that occurs in the overlap region of a crossbar consisting of two GNRs with one placed on top of the other at right angles. The GNRs in the crossbar are electronically decoupled from each other similar to the decoupling that occurs in twisted bilayer graphene. An analytical model based on Fermi's golden rule reveals that the decoupling is a consequence of the cancellation of quantum phases of the electronic states of the individual

GNRs. This leads to strong suppression of the inter-GNR transmission when the two GNRs are at the same potential. A potential difference between the GNRs changes the relative phases of the top and bottom wave functions and destroys the phase cancellation resulting in strong coupling and high transmission. Thus the transmission can be modulated several orders of magnitude by controlling the quantum phase using an external bias. A built-in potential between the two GNRs can lead to large peak-to-valley current ratios (>1000) resulting from the strong electronic decoupling of the two GNRs that occurs when they are driven to the same potential. Current switching by voltage control of the quantum phase in graphene crossbar structure is a novel switching mechanism. It is robust even with an overlap of ∼1.8 nm × 1.8 nm containing only ∼220 C atoms that is well below the smallest horizontal length scale envisioned in the ITRS.

ACKNOWLEDGMENT

This work is supported by the Microelectronics Advanced Research Corporation Focus Center on Nano Materials (FENA).

*khabib@ee.ucr.edu
†rlake@ee.ucr.edu

[1] K. S. Novoselov, A. K. Geim, S. V. Morozov, D. Jiang, M. I. Katsnelson, I. V. Grigorieva, S. V. Dubonos, and A. A. Firsov, Nature (London) **438**, 197 (2005).
[2] T. Ando, Physica E **40**, 213 (2007).
[3] D. C. Elias *et al*., Science **323**, 610 (2009).
[4] X. Li, X. Wang, L. Zhang, S. Lee, and H. Dai, Science **319**, 1229 (2008).
[5] K.-T. Lam and G. Liang, Appl. Phys. Lett. **92**, 223106 (2008).
[6] M. Y. Han, B. Özyilmaz, Y. Zhang, and P. Kim, Phys. Rev. Lett. **98**, 206805 (2007).
[7] C. L. Lu, C. P. Chang, Y. C. Huang, J. M. Lu, C. C. Hwang, and M. F. Lin, J. Phys.: Condens. Matter **18**, 5849 (2006).
[8] H. Min, B. Sahu, S. K. Banerjee, and A. H. MacDonald, Phys. Rev. B **75**, 155115 (2007).
[9] Y. Zhang, T.-T. Tang, C. Girit, Z. Hao, M. C. Martin, A. Zettl, M. F. Crommie, Y. R. Shen, and F. Wang, Nature (London) **459**, 820 (2009).
[10] M. Gilbert, Electron Devices, IEEE Trans. **57**, 3059 (2010).
[11] S. K. Banerjee, L. F. Register, E. Tutuc, D. Reddy, and A. H. MacDonald, IEEE Electron Device Lett. **30**, 158 (2009).
[12] L. Britnell *et al*., Science **335**, 947 (2012).
[13] Y. Yoon and S. Salahuddin, Appl. Phys. Lett. **97**, 033102 (2010).
[14] R. M. Feenstra, D. Jena, and G. Gu, J. Appl. Phys. **111**, 043711 (2012).
[15] T. Sohier and B. Yu, Appl. Phys. Lett. **98**, 213104 (2011).
[16] V. H. Nguyen, A. Bournel, and P. Dollfus, Appl. Phys. Lett. **109**, 093706 (2011).
[17] V. N. Do and P. Dollfus, J. Appl. Phys. **107**, 063705 (2010).
[18] H. Ren, Q.-X. Li, Y. Luo, and J. Yang, Appl. Phys. Lett. **94**, 173110 (2009).
[19] K. M. M. Habib, F. Zahid, and R. K. Lake, Appl. Phys. Lett. **98**, 192112 (2011).
[20] International Technology Roadmap for Semiconductors 2011, edited by Emerging Research Devices (ERD). [http://www.itrs.net/Links/2011ITRS].
[21] X. Wu, X. Li, Z. Song, C. Berger, and W. A. de Heer, Phys. Rev. Lett. **98**, 136801 (2007).
[22] J. Hass, F. Varchon, J. Millán-Otoya, M. Sprinkle, N. Sharma, W. de Heer, C. Berger, P. First, L. Magaud, and E. Conrad, Phys. Rev. Lett. **100**, 125504 (2008).
[23] S. Latil, V. Meunier, and L. Henrard, Phys. Rev. B **76**, 201402(R) (2007).
[24] S. Shallcross, S. Sharma, and O. A. Pankratov, Phys. Rev. Lett. **101**, 056803 (2008).
[25] S. Shallcross, S. Sharma, E. Kandelaki, and O. A. Pankratov, Phys. Rev. B **81**, 165105 (2010).
[26] B. Lopes dos Santos J. M., R. Peres N. M., and H. CastroNeto A., Phys. Rev. Lett. **99**, 256802 (2007).
[27] A. Luican, G. Li, A. Reina, J. Kong, R. R. Nair, K. S. Novoselov, A. K. Geim, and E. Y. Andrei, Phys. Rev. Lett. **106**, 126802 (2011).
[28] E. Suárez Morell, P. Vargas, L. Chico, and L. Brey, Phys. Rev. B **84**, 195421 (2011).
[29] L. Xian, S. Barraza-Lopez, and M. Chou, Phys. Rev. B **84**, 075425 (2011).
[30] R. Bistritzer and H. MacDonald A., Phys. Rev. B **81**, 245412 (2010).
[31] L. Jiao, L. Zhang, L. Ding, J. Liu, and H. Dai, Nano Research **3**, 387 (2010).
[32] A. R. Botello-Mendez, E. Cruz-Silva, J. M. Romo-Herrera, F. Lopez-Urias, M. Terrones, B. G. Sumpter, H. Terrones, J.-C. Charlier, and V. Meunier, Nano Lett. **11**, 3058 (2011).
[33] M. Hanggi and L. O. Chua, Intl. J. Cir. Th. App. **29**, 487 (2001).
[34] K. M. M. Habib, A. Khitun, A. A. Balandin, and R. K. Lake, in *2011 IEEE/ACM International Symposium on Nanoscale Architectures (NANOARCH)* (2011), pp. 86–90.
[35] S. Khasanvis, K. M. M. Habib, M. Rahman, P. Narayanan, R. K. Lake, and C. A. Moritz, in *2011 IEEE/ACM International Symposium on Nanoscale Architectures (NANOARCH)* (2011), pp. 189–195.
[36] O. F. Sankey and D. J. Niklewski, Phys. Rev. B **40**, 3979 (1989).
[37] J. P. Lewis, K. R. Glaesemann, G. A. Voth, J. Fritsch, A. A. Demkov, J. Ortega, and O. F. Sankey, Phys. Rev. B **64**, 195103 (2001).
[38] Y.-W. Son, M. L. Cohen, and S. G. Louie, Phys. Rev. Lett. **97**, 216803 (2006).
[39] J. P. Lewis *et al*., Phys. Status Solidi B **248**, 1989 (2011).
[40] J. L. Martins, N. Troullier, and S. H. Wei, Phys. Rev. B **43**, 2213 (1991).
[41] A. D. Becke, Phys. Rev. A **38**, 3098 (1988).
[42] C. Lee, W. Yang, and R. G. Parr, Phys. Rev. B **37**, 785 (1988).
[43] J. Harris, Phys. Rev. B **31**, 1770 (1985).
[44] W. M. C. Foulkes and R. Haydock, Phys. Rev. B **39**, 12520 (1989).
[45] A. A. Demkov, J. Ortega, O. F. Sankey, and M. P. Grumbach, Phys. Rev. B **52**, 1618 (1995).
[46] O. F. Sankey, A. A. Demkov, W. Windl, J. H. Fritsch, J. P. Lewis, and M. Fuentes-Cabrera, Int. J. Quantum Chem. **69**, 327 (1998).

[47]P. Jelinek, H. Wang, J. P. Lewis, O. F. Sankey, and J. Ortega, Phys. Rev. B **71**, 235101 (2005).
[48]N. A. Bruque, M. K. Ashraf, T. R. Helander, G. J. O. Beran, and R. K. Lake, Phys. Rev. B **80**, 155455 (2009).
[49]J. Tomfohr and O. F. Sankey, J. Chem. Phys. **120**, 1542 (2004).
[50]M. Galperin, S. Toledo, and A. Nitzan, J. Chem. Phys. **117**, 10817 (2002).
[51]H. Zheng, Z. F. Wang, T. Luo, Q. W. Shi, and J. Chen, Phys. Rev. B **75**, 165414 (2007).
[52]B. Huard, J. A. Sulpizio, N. Stander, K. Todd, B. Yang, and D. Goldhaber-Gordon, Phys. Rev. Lett. **98**, 236803 (2007).
[53]L. M. Zhang and M. M. Fogler, Phys. Rev. Lett. **100**, 116804 (2008).
[54]D. B. Farmer, Y.-M. Lin, A. Afzali-Ardakani, and P. Avouris, Appl. Phys. Lett. **94**, 213106 (2009).
[55]K. Brenner and R. Murali, Appl. Phys. Lett. **96**, 063104 (2010).